Chemical Engineering Journal 483 (2024) 149134

Contents lists available at ScienceDirect

Chemical Engineering Journal

journal homepage: www.elsevier.com/locate/cej

Surface hydrophobicity of boron nitride promotes PFOA photocatalytic degradation

Bo Wang [a,b,1], Yu Chen [a,b,1], Joshua Samba [b,c], Kimberly Heck [a,b], Xiaochuan Huang [b,d], Junseok Lee [b,f], Jordin Metz [b,e], Manav Bhati [a,b], John Fortner [b,f], Qilin Li [a,b,d], Paul Westerhoff [b,g], Pedro Alvarez [a,b,d,e,h], Thomas P. Senftle [a,b,*], Michael S. Wong [a,b,d,e,h,*]

[a] Department of Chemical and Biomolecular Engineering, Rice University, Houston, TX 77005, USA
[b] Nanosystems Engineering Research Center for Nanotechnology-Enabled Water Treatment, Houston, TX 77005, USA
[c] Applied Physics Graduate Program, Rice University, Houston, TX 77005, USA
[d] Department of Environmental Engineering, Rice University, Houston, TX 77005, USA
[e] Department of Chemistry, Rice University, Houston, TX 77005, USA
[f] Department of Chemical and Environmental Engineering, Yale University, New Haven, CT, USA
[g] School of Sustainable Engineering and Built Environment, Arizona State University, Tempe, AZ 85281, USA
[h] Department of Materials Science and NanoEngineering, Rice University, Houston, TX 77005, USA

A B S T R A C T

Boron nitride (BN) photodegrades perfluorooctanoic acid (PFOA) in water under 254-nm light illumination more rapidly than TiO_2, which is hypothesized due to its greater surface hydrophobicity. We investigated the role of hydrophobicity on PFOA photocatalysis by comparing BN with anatase TiO_2 under reaction conditions, for which the exposed surface areas were the same. BN exhibited ~ 3.5 × faster PFOA degradation rate compared to TiO_2 under acidic pH conditions. PFOA adsorption experiments showed that BN had ~ 2 × higher PFOA surface coverage, consistent with its higher surface hydrophobicity, as corroborated by contact angle measurements. Both materials were comparatively less photocatalytically active at neutral pH, but BN still exhibited ~ 2.7 × faster PFOA degradation rate, due to less electrostatic attraction between the PFOA headgroup and the catalyst surface. Langmuir-Hinshelwood rate law analysis suggests BN and TiO_2 have comparable photogenerated hole surface concentrations, and density functional theory calculations show that the holes for both photocatalysts can react with surface hydroxyls and with adsorbed PFOA. However, BN has comparatively less surface hydroxyl groups and more adsorbed PFOA, which favors hole reaction with the latter, resulting in a higher PFOA degradation rate. These insights into the role of surface hydrophobicity serve as rationally-guided design principles for improved heterogeneous photocatalysis of persistent surfactants, including the broad suite of per- or poly-fluoroalkyl substances.

1. Introduction

Per- and poly-fluoroalkyl substances (PFAS), or “forever chemicals,” are a group of anthropogenic fluorinated organic compounds which have been widely used industrially and in consumer products to take advantage of their unique properties, including chemical/thermal stability, surfactant properties, and hydrophobic/lipophobic nature [1]. Perfluorooctanoic acid (PFOA), one of the most regulated and investigated PFAS representatives, had a global output of 3600—5700 t from 1951 to 2004, of which about 400—700 t was directly discharged into the environment [2]. PFAS contamination has been globally detected in soil, plant, rainwater, surface water, and groundwater, including many drinking water supplies [3–6]. The stability of C-F bonds and the surfactant properties of PFAS lead to incomplete removal by standard water treatment methods, and ppb (μg/L) levels of PFAS have been detected in human tissues and blood serum [7,8]. Exposure to parts-per-quadrillion of PFAS in water has negative health effects, including kidney, liver, and reproductive problems in adults, suppressed immune response to vaccines, and neurological/behavioral issues in children [9,10]. Regulations are coming to push to solve these “forever” chemical problems. The United States Environmental Protection Agency (U.S. EPA) released a PFAS Strategic Roadmap in Oct 2021, which set timelines by which EPA plans to take specific actions and commit to bolder new policies to safeguard public health and protect the environment. In March 2023, the U.S. EPA proposed Federal Maximum Contaminant Levels (MCLs) for six PFAS in drinking water. The proposed MCL for

* Corresponding authors at: Department of Chemical and Biomolecular Engineering, Rice University, Houston, TX 77005, USA; Nanosystems Engineering Research Center for Nanotechnology-Enabled Water Treatment, Houston, TX 77005, USA (T.P. Senftle and M.S. Wong)
E-mail addresses: tsenftle@rice.edu (T.P. Senftle), mswong@rice.edu (M.S. Wong).
[1] These authors contributed equally to the manuscript.

https://doi.org/10.1016/j.cej.2024.149134
Received 16 August 2023; Received in revised form 20 January 2024; Accepted 25 January 2024
Available online 1 February 2024

PFOA and PFOS are 4 ppt (=4 ng/L), and a Hazard Index MCL was proposed for the sum of four other PFAS (PFNA, GenX chemicals, PFHxS, and PFBS) that accounts for their varying relative health risks. The European Chemicals Agency also proposed to reduce and ban the production and use of ~ 10,000 PFAS in the European Union [11].

Semiconductor-based photocatalysts have shown great potential for destroying PFOA contaminated waters [12–17]. We previously reported that the semiconductor material, boron nitride (BN), photocatalytically oxidized and degraded PFOA under 254-nm light illumination ~ 4 × faster than TiO_2 [18]. BN is a commercially available [19–21], nontoxic, and earth-abundant element-containing material used in cosmetics, dental cement, and paint [22]. The ability of BN to act as a photocatalyst is unexpected because of its wide band gap and chemical inertness. Density of states (DOS) analysis conducted by Salavati-Fard and Wang indicated that the existence of point defects was essential to activate BN for photocatalytic reactions [23]. Our recent density functional theory (DFT) calculations showed nitrogen-at-boron-site substitutional defects (N_B) generated a mid-gap state that enabled BN to absorb 254-nm light [24]. We confirmed the thermodynamic and kinetic favorability of the direct oxidation of PFOA by the photogenerated holes (delocalized over the non-defect N atoms of BN), [24] which is the first step in the DHEH (decarboxylation-hydroxylation-elimination-hydrolysis) reaction pathway generally accepted for other semiconductor photocatalysts like TiO_2, [15] In_2O_3, [14,25,26] and BiOCl [27].

The hydrophobic nature of BN surfaces very likely contributes to its superior PFOA photodegradation activity also, but this effect has not yet been rigorously studied. We previously observed that shorter-chain perfluorocarboxylic acid (PFCA) byproducts generated from incomplete PFOA photodegradation took longer to degrade, [18] consistent with reports of other photocatalytic materials [28,29]. Our DFT calculations indicated shorter-chain PFCAs only weakly adsorbed to the surface, as a result of decreased interactions of the tail group with the hydrophobic BN surface [24]. PFCAs behave less like surfactant molecules as the hydrocarbon tail shortens [30,31]. We infer that the surface coverage of the more hydrophilic shorter-chain PFCAs is lower compared to PFOA surface coverage, which would decrease opportunities for shorter-chain PFCAs to react with photogenerated holes on the BN surface.

Here, we investigated the surface hydrophobicity of BN on PFOA photocatalysis by comparing it with hydrophilic TiO_2. We performed PFOA adsorption isotherm measurements for BN for the first time, with pH effects consistent with anion adsorption on charged surfaces. We compared photocatalytic activity of the two materials with the same exposed surface area, and performed hole scavenger experiments, reactive oxygen species (ROS) quantification, and DFT calculations. Through a comparative Langmuir-Hinshelwood rate law analysis, we discussed the factors that contributed to differences in reaction rates between BN and TiO_2. We identified several ways in which surface hydrophobicity benefited PFAS photocatalytic oxidation, which can help the design and engineering of improved catalysts for targeted PFAS degradation.

2. Experimental and DFT methods

2.1. Materials

All materials were of analytical grade and used as received. Perfluorooctanoic acid (PFOA, $C_7F_{15}COOH$, 96 % purity) and anatase-TiO_2 were obtained from Sigma-Aldrich, and BN was obtained from 3 M company. Ethylenediaminetetraacetate disodium salt dihydrate (EDTA•2Na, 99 % purity) was obtained from Sigma-Aldrich. Disodium terephthalate (TA•2Na, 99 % purity) was acquired from Alfa Aesar. The water used in all experiments was deionized (18.2 MΩ).

2.2. Characterization

The hexagonal phase of BN and anatase phase of TiO_2 were confirmed using X-ray powder diffraction (XRD, Fig. S1). The information of particle size, purity, and market price obtained from the manufacturer and the elemental compositions obtained using X-ray photoelectron spectroscopy with a PHI Quantera System are provided in Fig. S1. Multipoint (10 points) nitrogen physisorption was performed on the samples following 5 h of evacuation at 150 °C and the specific surface areas (S_{BET}) were determined using the Brunauer–Emmett–Teller (BET) equation (S_{BET} of 40 m^2/g-BN and 100 m^2/g-TiO_2). The XPS spectra and the peak deconvolution results were corrected using the C 1 s peak at 284.6 (Fig. S3).

Diffuse reflectance infrared Fourier transform spectroscopy (DRIFTS) experiments were performed on a Thermo Scientific Nicolet iS10 FTIR spectrometer equipped with a liquid-N_2-cooled HgCdTe (MCT) detector (Fig. S2). A high-temperature reaction chamber equipped with ZnSe windows, mounted on a Praying Mantis diffuse reflectance accessory (Harrick Scientific), was used for DRIFTS analysis of the samples at 25 °C under He atmosphere at 10 torr total pressure. Before being placed in the reaction chamber, samples were diluted to 10 wt% in KBr. Temperature was monitored by positioning a type-K thermocouple in the sample cup and controlled using an ATK temperature controller (Harrick Scientific). Pure KBr was used as a background spectrum for all samples. All spectra are reported in Kubelka-Munk units by averaging 128 scans at 4 cm^{-1} resolution.

The hBN or Anatase TiO_2 powder was put into a customized sample holder (Scheme S1) and pressed under 2.4 MPa for 45 s using a bench top hydraulic press (Model 4389, Carver, Inc, USA) to form pellets, which were then used for contact angle measurement. A goniometer (DAS100, KRUSS) was used to measure the contact angles of DI water on BN and TiO_2; five measurements were made on each sample and the average value was reported (standard deviation < 2 %). The zeta potential measurement of BN and TiO_2 were determined with a Brookhaven Instruments ZetaPALS with BI-9000AT digital autocorrelator using 1.6 mL aqueous slurry (0.25 mg/mL) at various pH conditions (pH 2–8), which was adjusted using 0.1 M HCl and NaOH solutions.

2.3. PFOA adsorption kinetics and isotherm measurements

Sorption kinetic experiments were conducted by adding 1.25 g/L BN or 0.5 g/L of TiO_2 to a 500 mL polypropylene bottle containing 400 mL of 50 mg/L (120 μM) PFOA solution with the initial pH adjusted to 3.5 or 6.8. The bottles were mechanically shaken at 25 °C and 150 rpm with aliquots taken out periodically. Each kinetic experiment was run in duplicate and the average value of the PFOA sorption amount was reported. For a given point, measured values differed by no more than 1 %.

The transient sorption kinetics were evaluated to estimate the equilibration time for each material and determine the initial sorption rate (v_0). The data was fitted using the pseudo-second-order kinetic model in Eq. (1):

$$\frac{t}{q_t} = \frac{1}{v_0} + \frac{t}{q_e} \quad (1)$$

where q_e and q_t are the amounts of PFOA adsorbed at equilibrium (mmol/m^2) and at time t, and v_0 is the initial sorption rate (mmol/m^2/min). The time to reach PFOA adsorption equilibrium was determined to be ~ 20 min (Fig. S4).

Batch adsorption isotherm experiments were conducted in 50-mL polypropylene centrifuge tubes containing 40 mL of a PFOA solution ranging from 25 to 480 μM (10–200 mg/L). The sorbent loadings were 1.25 g/L for BN or 0.5 g/L for TiO_2 and the initial pH was 3.5 or 6.8. Each adsorption measurement was taken after 1 h of mechanical shaking.

The Langmuir model was used to determine PFOA surface coverage

(θ_{PFOA}):

$$\theta_{PFOA} = \frac{C_{PFOA,ad}}{C_m} = \frac{q_e}{q_m} = \frac{bC_e}{1+bC_e} \quad (2)$$

where $C_{PFOA,ad}$ is surface concentration of the adsorbed PFOA at equilibrium (μmol/m^2), C_m is the maximum PFOA sorption amount (μmol/m^2), C_e is the PFOA equilibrium concentration (μM), and b is the adsorption equilibrium constant (L/mmol). The linearized mathematical form of the Langmuir model is

$$\frac{C_e}{C_{PFOA,ad}} = \frac{C_e}{C_m} + \frac{1}{b \times C_m} \quad (3)$$

2.4. Photocatalytic testing

Photocatalytic reactions were conducted in a UV photoreactor system (equipped with six 4 W UVC Ushio G4T5 low pressure Hg germicidal lamps for the 254-nm UVC experiments) as in our previous work [18,32,33]. The photon flux measured by chemical actinometry was 6.5 × 10^{-6} Einstein·L^{-1}·s^{-1}, and the spectral irradiance was calculated to be 4.33 mW/cm^2. In a typical experiment, the photocatalysts (BN or TiO_2) and 120 μM (50 mg/L) PFOA were added to a 100-mL flask quartz reactor with 20-mL DI water and adjusted to either pH 3.5 using HCl or pH 6.8 using NaOH. Based upon our prior screening, the catalyst concentration of 0.5 g/L of TiO_2 was determined to be within the optimum dosage range, such that higher concentrations did not increase (or decrease, due to decreased light penetration through the reaction volume) the observed photocatalytic degradation [18,32]. The amount of BN charged to the batch reactor was 1.25 g/L, such that the total surface area (1 m^2, based on BET-calculated specific surface areas) was equal to the TiO_2 case.

The reactor was sealed with ambient air and then stirred for 30 min in the dark to ensure PFOA adsorption reached equilibrium before light irradiation. During reaction, samples were withdrawn over time and filtered with 0.22-μm polyethersulfone (PES) syringe filters before analysis. PES filters were used, due to their lack of adsorption of PFOA and PCFA's [34]. All experiments were repeated in triplicate.

2.5. Reaction fluid analytical methods

PFOA concentrations were measured via high-performance liquid chromatography (HPLC, 1260 Infinity II Agilent, USA) with an Agilent WPH C18 column (4.6 mm × 250 mm, 5 μm). The mobile phase was acetonitrile and 5 mM Na_2HPO_4 with a volume ratio of 50:50 (v/v), the flow rate was 0.8 mL·min^{-1}, the temperature of the column was 30 ℃, the sample injection volume was 50 μL, and a UV detector with a wavelength 210 nm was used. The detection limit for PFOA was ~ 2.5 μM (1 mg/L). The released fluoride ion concentration was analyzed by ion chromatography (IC) with suppressed conductivity detection (Dionex Aquion, 4 × 250 mm IonPac AS23, AERS 500 Carbonate Suppressor). pH measurements were recorded using an Orion Star A111 pH probe.

HPLC was used to quantify EDTA consumption in experiments to assess photogeneration of holes during photocatalysis. The experiments were conducted in the same reactor and the same liquid volume (20 mL) and PFOA concentration (~120 μM) at pH 3.5 and 6.8, except for the addition of EDTA•Na for a final concentration of 3 mM (at 25 × higher concentration than PFOA). The detailed EDTA quantification method using HPLC can be found here [35,36].

To estimate hydroxyl radical (•OH) formation during photocatalysis, a fluorescent assay based on terephthalic acid (TA) as the radical trap was used. These experiments were conducted in the same reactor and the same liquid volume (20 mL) and PFOA concentration (~120 μM) at pH 3.5, except for the addition of TA•2Na for a final concentration of 3 mM. More details of this assay can be found in our previous work [37].

2.6. DFT settings

DFT was used to compute band edge positions and redox potentials of proposed oxidation reaction steps. These calculations were used to assess reaction favorability, as a reaction step with a less positive oxidation potential than the valence band maximum (VBM) is thermodynamically favorable. VASP 5.4.4 [38,39] was used in conjunction with VASPsol implicit solvation [40,41]. Band edge positions were determined using the method from Toroker *et al.* [42] The methodology for computing the oxidation potentials referenced to the standard hydrogen electrode (SHE) was described in our previous work [24]. Full calculation details and settings are provided in Appendix A.

The oxidation potential for the formation of the •OH radical from a surface-adsorbed hydroxide in the anatase TiO_2 system was computed using Eq. (4),

$$OH^* + h^+ \rightarrow \cdot OH + *(+1) \quad (4)$$

where OH* represents a hydroxide adsorbed on the surface, h^+ represents a hole, •OH represents a hydroxyl radical in solution, and * represents the + 1 charged TiO_2 surface with the OH* adsorption site vacated.

The OH* adsorption configuration was modeled as an anatase TiO_2 (1 0 1) surface covered with a 50 % dissociated water layer (Fig. S6a), where the overall system charge was neutral since each adsorbed hydroxide is compensated by an adsorbed proton. This choice of water layer and anatase surface structure used in this work is justified by both experimental and theoretical results from the literature. The presence of OH* groups bound to surface Ti atoms was confirmed by surface x-ray diffraction results from Nadeem et al. [43] Martinez-Casado et al. [44] analyzed the anatase (1 0 1) surface interaction with water using DFT and found that ~ 50 % water dissociation is favorable. Walle et al. [45] investigated the surface coverage of OH* under different temperatures and reported a ~ 0.47 mono-layer of OH* on the surface. The *(+1) structure consists of the same surface model but with one OH* group removed from the surface yielding a net charge of + 1 $|e|$ in the surface slab model (Fig. S6b). The charged slab in is balanced by the ion distribution in the VASPsol implicit solvation model [40,41] to yield an overall neutral cell. •OH was treated in an isolated simulation cell with VASPsol implicit solvation. A •OH concentration of 2.5 × 10^{-4} M (determined from the experiments described Section 3.5) was used to compute the free energy •OH, which in turn is used to calculate the redox potential according to Eqns. S4–S5.

For the BN system, the oxidation potential for the formation of the •OH radical from a surface hydroxide was computed using Eq. (5),

$$OH^*(-1) + h^+ \rightarrow \cdot OH + * \quad (5)$$

OH*(-1) represents a $–OH^-$ group on a four-coordinated boron site of the BN armchair edge with B-O and B-OH terminations (Fig. S6c). This edge model was motivated by experimental characterization reported by Dorn et al. [46] OH*(-1) is in the −1 $|e|$ charge state to account for the negatively charged 4-coordinated boron species, * represents a neutral armchair edge defect with three-coordinated B-O and B-OH terminations (Fig. S6d). [46] A •OH concentration of 5 × 10^{-5} M (determined from the experiments described Section 3.5) was used to calculate the redox potential using Eqns. S4–S5.

The redox potential for the formation of the •OH radical from a water molecule (2.63 V_{SHE}) via Eq. (6) was calculated using Eqns. S9–S10.

$$H_2O + h^+ \rightarrow \cdot OH + H^+ \quad (6)$$

This potential was calculated to determine the possibility of direct water oxidation. The computed value compares well with the experimental value of 2.73 V_{NHE} [47].

The oxidation potentials for the PFCA anion to form of a perfluorocarboxyl radical (2.17 V_{SHE}) via Eq. (7) or to simultaneously form

a perfluoroalkyl radical and 1 atm gas-phase carbon dioxide (1.17 V_{SHE}) via Eq. (8) was computed using Eqns. S4 and S5,

$$CF_3CF_2COO^- + h^+ \rightarrow CF_3CF_2COO\cdot \quad (7)$$

$$CF_3CF_2COO^- + h^+ \rightarrow CF_3CF_2\cdot + CO_2(g) \quad (8)$$

The calculated redox potentials of PFCAs do not depend significantly on PFCA chain length, [24] so we used a model C3 PFCA anion in this study for computational efficiency. The anionic, deprotonated form of the PFCA molecule was employed because the pH in the PFOA degradation experiments was always much higher than the pK_a of PFOA (~0) [48].

3. Results and discussion

3.1. BN has a higher PFOA photodegradation rate than TiO_2 at different pH values

The mass loadings of BN and TiO_2 powders charged to the batch reactor were such that the total surface area exposed in the reaction fluid was the same, to account for materials with different specific surface areas during photocatalytic measurements. We adjusted the pH of the reaction mixture with HCl to 3.5, to match the end-of-reaction pH value observed with the near-neutral pH experiments described later. The observed PFOA solution concentration decreases after 30 min of contact time in the dark (from 120 μM to ~ 112 and ~ 118 μM for BN and TiO_2, respectively, Fig. 1a) corresponded to the equilibrium PFOA sorption capacities for BN and TiO_2 of 0.2 and 0.1 μmol/m^2, respectively (Fig. S4).

After pre-equilibration in the dark and with time t = 0 min marking the start of the 254-nm illumination, PFOA concentrations continuously decreased for both materials (Fig. 1a). After 720 min of reaction time, the PFOA concentration dropped below the detection limit (7 μM, corresponding to 1 ppm) for the BN case, and to ~ 45 μM for the TiO_2 case. The initial reaction rates (determined from the first 120 min) were calculated as 0.171 μM PFOA/min and 0.049 μM PFOA/min, indicating BN was ~ 3.5 × more active than TiO_2. Fluoride ions were detected after irradiation began, indicative of C-F bond cleavage (Fig. 1b). Defluorination extent (percentage of the total fluorine added to the reactor detected as fluoride ions) was 22 % and 16 % for BN and TiO_2, respectively, at the end of 720 min reaction time. Defluorination did not reach 100 % (equivalent to ~ 1800 μM of fluoride), due to formation of shorter-chain PFCA [18,49].

We carried out the testing procedure again but at near-neutral pH (6.8), by adding NaOH to the PFOA/catalyst reaction mixtures. PFOA adsorption also occurred in the dark, but the equilibrium sorption amounts were lower (0.11 μmol/m^2 and 0.04 μmol/m^2, respectively, for BN and TiO_2) were lower than those at acidic conditions. Upon illumination, both PFOA concentration and solution pH decreased, and the final pH was 3.5 after 12 h for the BN case resulting from H^+ formation [18,32]. The pH decreased to a lesser degree (from 6.8 to 5.5) for TiO_2, which is reflective of lower PFOA degradation extent. Defluorination was 11 % and 3 %, respectively, for BN and TiO_2, comparatively less than the pH 3.5 cases (Fig. 1b). Initial degradation reaction rates (0.057 and 0.021 μM PFOA/min, for BN and TiO_2, respectively) were also comparatively lower. Overall, we quantitatively find that BN is roughly 2.7–3.5 × more active than TiO_2, and that lower pH values promote both PFOA photocatalytic degradation and PFOA adsorption.

3.2. BN adsorbs more PFOA than TiO_2 does

We quantified PFOA adsorption on BN and TiO_2 at the two pH values at which photocatalysis was performed. Fig. 2 **a&b** shows the adsorption isotherms, where the equilibrium data fit well to a Langmuir adsorption model (Eq. (2)), implying that PFOA adsorbs as a monolayer on both BN and TiO_2 [50].

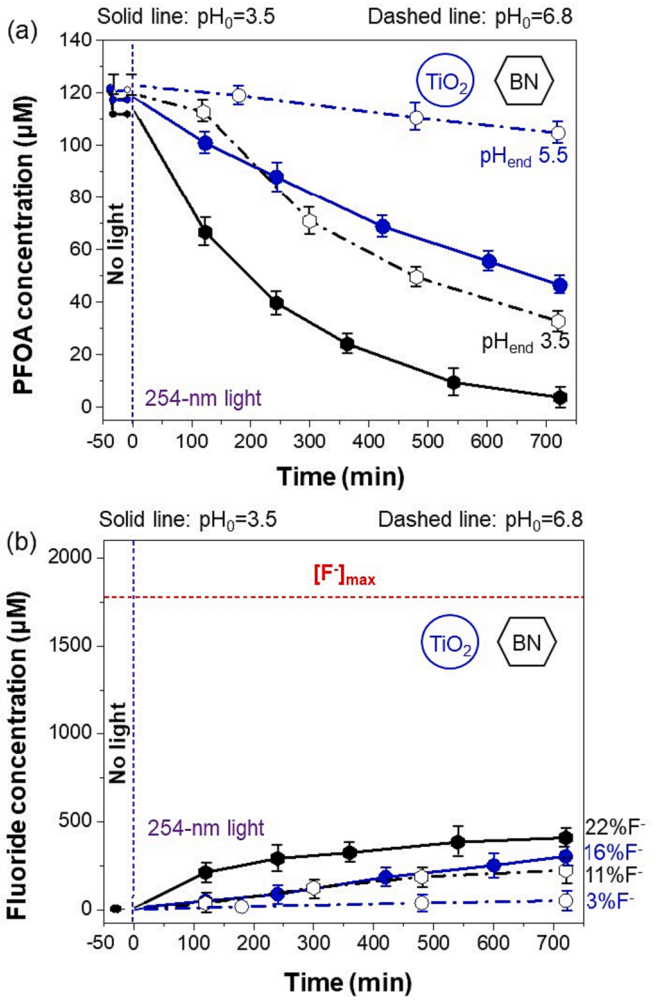

Fig. 1. (a) HPLC-DAD detected PFOA concentration–time profiles and (b) fluoride concentration–time profiles over BN and TiO_2 at pH 3.5 and 6.8 with 254-nm irradiation. Reaction conditions: [PFOA] (at t = -30 min) = ~120 μM (~50 ppm), catalyst charge with total surface area of 1 m^2 for BN (1.25 g/L, S_{BET} = 40 m^2/g) and TiO_2 (0.5 g/L, S_{BET} = 100 m^2/g), 254-nm light, photon flux = 6.5 × 10^{-6} Einstein·L^{-1}·s^{-1} (2.92 × 10^{14} photons·s^{-1}·cm^{-2}), initial pH = 3.5 or 6.8, ambient temperature, air headspace.

The calculated PFOA monolayer adsorption capacity (C_m) and adsorption equilibrium constant (b) of anatase under acidic conditions were similar to previous results reported for TiO_2 P25 (Table 1) [51]. BN and TiO_2 have similar adsorption capacity due to the same total expose surface area in water, but the adsorption equilibrium constant of BN was ~ 2 × higher than TiO_2 under acidic conditions. At neutral pH, both C_m and b values decreased for both BN and TiO_2, indicative of pH-dependent charge interactions between the surfaces and PFOA. At both pH values, the PFOA surface coverage, θ_{PFOA}, of BN was almost twice that of TiO_2 (0.26 *v.* 0.14, and 0.25 *v.* 0.12).

3.3. BN surface is charged, hydrophobic, and water-wettable

We determined the effective surface charges of BN and TiO_2 suspended in water as a function of pH via zeta potential measurements (Fig. 3). The zeta potential of BN was + 5 mV at the lowest pH tested, and it decreased with increasing pH, such that zeta potential reached zero at a pH around 2.9. This point of zero charge (PZC) is consistent with previous reports [52,53]. Above this PZC, the BN surface became increasingly negatively charged with increasing pH, due to deprotonation of surface hydroxyl groups (BN powders are slightly oxidized,

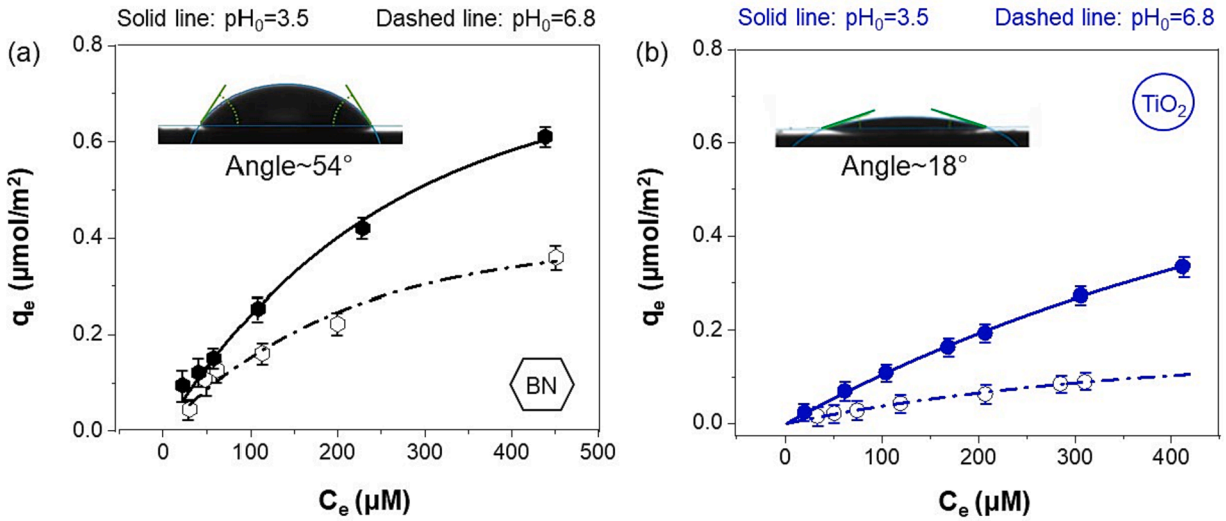

Fig. 2. PFOA sorption isotherms for (a) BN and (b) TiO_2 at pH 3.5 (solid line) and 6.8 (dashed line). C_e represents the equilibrium PFOA concentration in the solution phase and q_e represents the PFOA sorption amount. All isotherms fit well with a Langmuir model. Inset: Representative contact angle images for BN and TiO_2.

Table 1
Isotherm parameters for PFOA sorption over BN and TiO_2.

	Langmuir Constants (Eq. (3))			Surface Coverage at C_e ~ 120 μM (Eq. (2))
	C_m (μmol/m^2)	B (L/μmol)	R^2	θ_{PFOA}
BN-pH 3.5	1.19 ± 0.02	2.96 ± 0.06 × 10^{-3}	0.94	0.26
TiO_2-pH 3.5	1.13 ± 0.01	1.38 ± 0.01 × 10^{-3}	0.94	0.14
BN-pH 6.8	0.71 ± 0.01	2.63 ± 0.05 × 10^{-3}	0.96	0.25
TiO_2-pH 6.8	0.63 ± 0.01	1.14 ± 0.01 × 10^{-3}	0.93	0.12

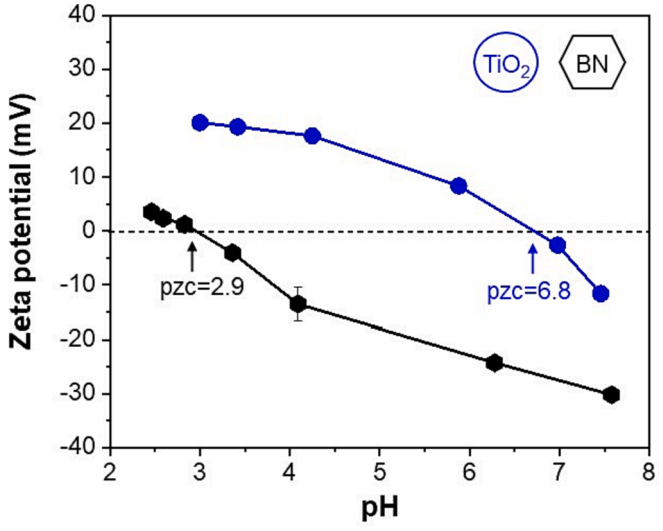

Fig. 3. Zeta potential measurements of BN and TiO_2 suspensions.

containing ~ 2 at% oxygen ~ 1.3 wt% oxygen, Fig. S3). In going from the photocatalytic reaction pH of 3.5 to 6.8, BN became more negatively charged, correlating to the observed lower PFOA adsorption (at pH 6.8).

The PZC of anatase was determined to be ~ 6.8, consistent with literature values [54,55]. The TiO_2 zeta potential became more positive in value with decreasing pH, corresponding to the observed higher PFOA adsorption at pH 3.5 than at pH 6.8. The anatase surface is positively charged, leading to electrostatic attraction to the PFOA carboxylate head group. In contrast, the BN surface and PFOA are negatively charged at these pH values and therefore expected to be electrostatically repelling, and yet PFOA adsorption is substantially higher compared to TiO_2.

This higher adsorption equilibrium constant of BN confirms PFOA adsorption is driven by hydrophobic interactions. The octanol/water partition coefficient (log K_{ow}) of PFCA's (in which K_{ow} represents the equilibrium concentration ratio of a PFCA in n-octanol and in water) increases with carbon length (and tail hydrophobicity); log K_{ow} for PFOA was determined experimentally to be 4.67 ± 0.26 by Xiang *et al.* [56] Generally, hydrophobic materials (through hydrophobic interactions with the C-F tail) adsorb more PFOA than hydrophilic materials (through electrostatic interactions with the solvated and charged head group). Hydrophobic materials including activated carbon-based materials, [57–59] polymers, [60–62] and covalent or metal–organic frameworks [63,64] have excellent PFOA adsorption, compared to silica and other hydrophilic adsorbents [65]. BN has been shown as an absorbent for hydrophobic compounds such as other PFAS (though not PFOA), [66] dyes, [67,68] and pharmaceuticals [69,70].

The hydrophobicity of BN is widely reported, [71–73] but its wettability by water depends on the form of the BN material and extent of surface oxidation. We conducted water contact angle measurements to compare the surface wettability of the BN and TiO_2 powders. BN had a contact angle of ~ 54° (Fig. 3a, **inset**), in good agreement with reported literature [72,74]. For comparison, the water contact angle for TiO_2 (a well-known hydrophilic material [75]) was much smaller (~18°) due to surface hydroxyl groups (Fig. 3b, **inset**) [43] They were detected on TiO_2 through DRIFTS (OH stretching in the 3000–4000 cm^{-1} range) but not on BN, indicating their relative paucity on the latter material (Fig. S2) [76]. Whereas pristine defect-free BN films have a much higher contact angle (~153°) [77] indicative of true hydrophobicity, the BN powder can be thought as agglomerated, surface-oxidized particles comprising stacks of two-dimensional BN sheets. This BN form has lower contact angles due to the presence of ionizable B-OH (and N-H) terminal groups at the sheet edges (Fig. S3), [78,79] enhancing material stability in water.

3.4. PFOA reaction rate dependence on the surface concentrations of PFOA and hole

We gained insights into the factors influencing the PFOA photo-

degradation rate by building on our recent modeling work [24] and treating the direct oxidation of PFOA with the photogenerated hole as a one-electron transfer from PFOA to the surface site (Eq. (9)). We model the reaction rate law (units of μM/min) as first-order dependent on surface concentration of the adsorbed PFOA ($C_{PFOA,ad}$, units of μmol/m^2) and surface concentration of photogenerated holes (C_{holes}, units of μmol/m^2) (Eq. (10)):

$$C_7F_{15}COO^-_{ad} + h^+ \xrightarrow{k_1} C_7F_{15}COO\cdot \quad (9)$$

$$-r_{PFOA} = k_1 \times C_{PFOA,ad} \times C_{holes} \quad (10)$$

Substituting Eq. (2) into Eq. (10), the PFOA initial photodegradation rate is expressed as:

$$-r_{PFOA} = k_1 \times \theta_{PFOA} \times C_m \times C_{holes} \quad (11)$$

The PFOA initial photodegradation rates over BN and TiO_2 are written as Eqns. 12–13:

$$-r_{PFOA,BN} = k_{1,BN} \times \theta_{PFOA,BN} \times C_{m,BN} \times C_{holes,BN} \quad (12)$$

$$-r_{PFOA,TiO_2} = k_{1,TiO_2} \times \theta_{PFOA,TiO_2} \times C_{m,TiO_2} \times C_{holes,TiO_2} \quad (13)$$

We sought to quantify the individual rate constants $k_{1,BN}$ and k_{1,TiO_2}(units of m^4/(μmol·L·min)), but the concentration of photogenerated hole is difficult to measure. Instead, we chose to determine the relative reaction ratio $k_{1,BN}/k_{1,TiO_2}$ from Eq. (14), assuming ratios of the other terms can be quantified or estimated.

$$\frac{-r_{PFOA,BN}}{-r_{PFOA,TiO_2}} = \frac{k_{1,BN}}{k_{1,TiO_2}} \times \frac{\theta_{PFOA,BN}}{\theta_{PFOA,TiO_2}} \times \frac{C_{m,BN}}{C_{m,TiO_2}} \times \frac{C_{holes,BN}}{C_{holes,TiO_2}} \quad (14)$$

To assess the concentration of the photogenerated hole, we carried out PFOA photocatalysis at pH 3.5 in the presence of the hole scavenger EDTA (at 25 × higher concentration than PFOA). As expected, PFOA degradation was inhibited completely in both cases (Fig. 4, **inset**).

Prior to light exposure, BN and TiO_2 adsorbed 0.4 and 1.8 μmol/m^2 of EDTA, respectively at pH 3.5. With pKa values of 0, 1.5, 2, and 2.66, a considerable portion of EDTA species carries a negative charge at pH 3.5, facilitating its adsorption onto positively charged TiO_2. In the case of BN, both EDTA and BN exhibit negative charges, leading to electrostatic repulsion that lessens the sorption of EDTA onto the BN surface. Once illumination began, EDTA concentrations decreased continuously (Fig. 4), indicating the EDTA-hole reaction (Eq. (15)).

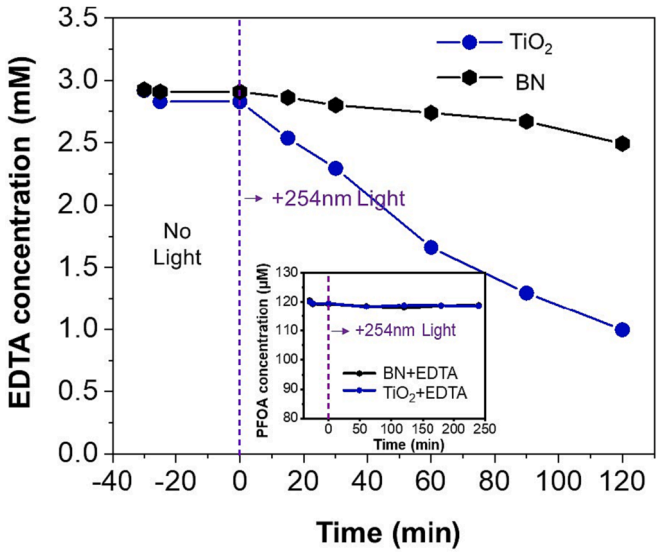

Fig. 4. EDTA concentration–time profiles and PFOA concentration–time profiles (inset), using EDTA as hole scavenger during PFOA photocatalysis with BN and with TiO_2. Reaction conditions: [EDTA] (at t = -30 min) = ~3 mM, [PFOA] (at t = -30 min) = 120 μM, same total surface area (1 m^2) of BN (1.25 g/L, S_{BET} = 40 m^2/g) or TiO_2 (0.5 g/L, S_{BET} = 100 m^2/g), ambient temperature, air headspace, initial pH 3.5, 254-nm light, photo flux = 6.5 × 10^{-6} Einstein·L^{-1}·s^{-1}.

$$EDTA_{ad} + h^+ \xrightarrow{k_{EDTA}} Product \quad (15)$$

The initial EDTA degradation rate was quantified as 4 and 20 EDTA/min for BN and TiO_2, respectively. EDTA was much slower to degrade over BN compared to TiO_2.

The EDTA initial photodegradation rates over BN and TiO_2 are then expressed as Eqns. 16–17.

$$-r_{EDTA,BN} = k_{EDTA,BN} \times C_{EDTA,ad,BN} \times C_{holes,BN} \quad (16)$$

$$-r_{EDTA,TiO_2} = k_{EDTA,TiO_2} \times C_{EDTA,ad,TiO_2} \times C_{holes,TiO_2} \quad (17)$$

where r_{EDTA} is the initial EDTA degradation rate (μM/min), k_{EDTA} is the effective reaction rate constant (μM/min), and C_{EDTA} is the adsorbed EDTA amount on the photocatalyst surface. The ratio of the EDTA degradation rates over the two materials is Eq. (18):

$$\frac{-r_{EDTA,BN}}{-r_{EDTA,TiO_2}} = \frac{k_{EDTA,BN}}{k_{EDTA,TiO_2}} \times \frac{C_{EDTA,ad,BN}}{C_{EDTA,ad,TiO_2}} \times \frac{C_{holes,BN}}{C_{holes,TiO_2}} \quad (18)$$

Fig. 4 results indicated that $\frac{C_{EDTA,ad,BN}}{C_{EDTA,ad,TiO_2}} = 0.22$ and $\frac{-r_{EDTA,BN}}{-r_{EDTA,TiO_2}} = 0.20$. An assumption in hole scavenging experiments is that EDTA reacts with holes indiscriminately, [80] the consequence of which is that EDTA reacts at same rate constant on both materials ($\frac{k_{EDTA,BN}}{k_{EDTA,TiO_2}} = 1$). While BN holes are different than TiO_2 holes, both are essentially unstable electron-deficient (N and O) atoms, and we do not expect their reactivity with EDTA to be significantly different. Substituting these values back into Eq. (18) allows us to estimate the $C_{holes,BN}/C_{holes,TiO_2}$ ratio to be 0.91.

With regard to the other terms of Eq. (14), Langmuir isotherm analysis indicated the PFOA surface coverage ratio $\theta_{PFOA,BN}/\theta_{PFOA,TiO_2}$ to be 1.85 (Table 1), and $\frac{C_{m,BN}}{C_{m,TiO_2}} = \frac{q_{m,BN}}{q_{m,TiO_2}}$ to be 1.05. The initial PFOA degradation rate ratio $\frac{-r_{PFOA,BN}}{-r_{PFOA,TiO_2}}$ was 3.50 (Fig. 1a). We thus estimated the rate constant ratio $k_{1,BN}/k_{1,TiO_2}$ to be 1.98, which indicated BN had twice the PFOA degradation rate constant as TiO_2 at 3.5. We performed the same analysis for the pH 6.8 case (slower PFOA degradation rates for both photocatalysts) and found BN had a slightly larger PFOA degradation rate constant (by 1.17 ×) than TiO_2 (Section S6). While it would be difficult to conclude that BN is intrinsically more photocatalytically active than TiO_2, the differences in rate constants suggest that there are other factors that contribute to BN's higher performance, after accounting for BN's greater PFOA adsorption (leading to higher PFOA surface coverage) and for comparable hole surface concentrations (as BN's smaller hole generation rate correlates to lower EDTA adsorption).

3.5. BN surface hydrophobicity and valence band position favor hole oxidation of PFOA over hole oxidation of water

Next, we considered that the hydrophobicity of the materials may affect PFOA degradation not only by adsorption, but in ways not typically considered. Photogenerated holes have been reported to oxidize surface hydroxyls from adsorbed water to form hydroxyl radicals (•OH) on TiO_2, [81,82] and the detection of hydroxyl radical (•OH) over photoexcited TiO_2 in aqueous environments has been widely reported [81,83,84]. Using electron paramagnetic resonance spectroscopy (EPR), Li *et al.* [26] found that photogenerated holes over TiO_2 are generally transformed into •OH radicals even in the presence of PFOA. On the other hand, BN, due to its hydrophobicity, does not form a significant amount of surface hydroxyls or adsorb a significant amount of water (as shown earlier in Fig. S2) [85]. We considered, then, that TiO_2's lower performance may not only be due to lower PFOA adsorption, but also due to the competition of PFOA with surface hydroxyls and/or adsorbed water to react with photogenerated holes.

Water dissociation over TiO_2 has been well studied, [43–45,86] and in these aqueous systems the TiO_2 surface would be hydroxylated. Surface hydroxyls could potentially be oxidized by photogenerated holes to form •OH (Eq. (4)). Through DFT analysis, we confirmed the thermodynamic favorability of this reaction by comparing its redox potential (1.95 V_{SHE}, red line in Fig. 5a) with the VBM of anatase TiO_2 with a dissociated water layer at pH = 6.8 (Fig. 5a). Since the position of the redox potential is above the edge of the valence band, it is thermodynamically favorable for the holes generated on TiO_2 to oxidize surface hydroxyls (OH^{-*}) to generate •OH (Fig. 5e). This implies holes are scavenged by the dissociated water layer, leaving fewer holes available to oxidize PFCA.

Also, the redox potentials of the reactions related to hole oxidation of PFCAs to form a perfluorocarboxyl radical (Eq. (7), Fig. 5c) or a decarboxylated perfluoroalkyl radical (Eq. (8), Fig. 5d) lie close to, and well above, the VBM of anatase, respectively, (the black and blue lines in Fig. 5a, respectively). Considering the redox potential calculation root mean square error (RMSE) of ± 0.2 V, we conclude that the oxidation of PFCA by a photo-generated hole on anatase TiO_2 is thermodynamically feasible but will compete with OH* oxidation.

By comparing the band edge alignment of BN (Fig. 5b) and the oxidation potential of Eq. (7) (2.17 V_{SHE}, black horizontal line in Fig. 5b) and Eq. (8) (1.17 V_{SHE}, blue horizontal line in Fig. 5b), we confirmed the thermodynamic feasibility of PFCA photo-oxidation over BN following PFCA adsorption. In our previous work [24], we examined the thermodynamic and kinetic favorability of PFCA activation via photo-oxidation on pristine BN by explicitly calculating its reaction energy and barrier over BN. The water oxidation potential of Eq. (6) (2.63 V_{SHE}, green line in Fig. 5b) is well below the VBM of BN positionally, indicating that holes would not be scavenged by intact water molecules near the BN basal plane. Therefore, under illumination, photogenerated holes would primarily react with PFOA due to BN's hydrophobicity (which promotes PFOA adsorption and excludes water on the BN basal plane).

We then examined the possible role of dissociated water on BN edge sites. Dorn *et al.* [46] characterized the edge termination of BN and found the edge is saturated by dissociated water, *i.e.*, BN's edges increase its hydrophilicity. Similar to the hydrophilic anatase surface, the dissociated water at the edge of BN could scavenge holes generated on BN and generate •OH. Previously, we found that the armchair edge defect with a four-coordinate boron featuring B-N, B-O, and 2 × B-OH coordination could be a source of •OH. [24] By comparing the redox potential of •OH generation (Eq. (5)) originated from OH* at the four-coordinate BN armchair edge (0.92 V_{SHE}, the orange horizontal line in Fig. 5b) with the VBM in Fig. 5b (the valence band edge of BN is not affected by the presence of the edge defects [24]), we find that the extra *OH group at the four-coordinated boron site is readily oxidized to form •OH by photogenerated holes, leaving behind the three-coordinated B site (Fig. 5f). Since the four-coordinated boron sites at the edge represent only a small fraction of exposed sites in the BN material, the •OH formation density in the BN system is expected to be much lower than on hydrophilic anatase.

To support the DFT findings, we performed additional experiments using terephthalic acid (TA) as a hydroxyl radical trap/scavenger during PFOA photocatalysis. PFOA degradation was partially inhibited over both BN and TiO_2 (Fig. 6 **inset**), confirming that hydroxyl radical participated in the PFOA degradation but to a smaller extent than the photogenerated holes. Previous reports showed •OH radicals cannot

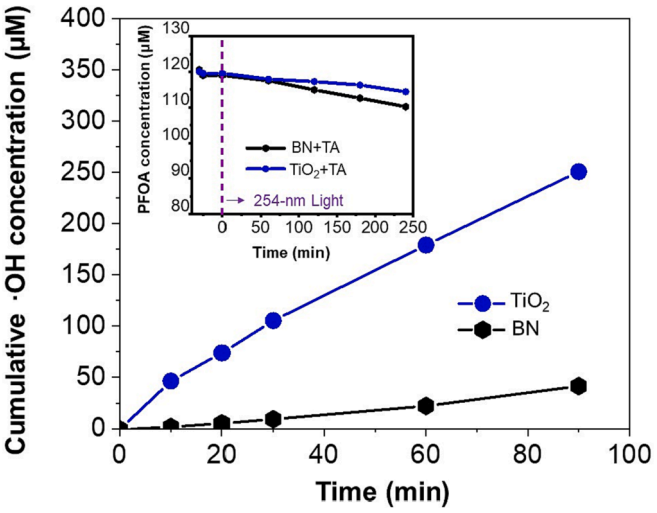

Fig. 6. Cumulative hydroxyl radical concentration–time profiles and PFOA concentration–time profiles (inset), using terephthalic acid as hydroxyl radical scavenger during PFOA photocatalysis with BN and with TiO_2. Reaction conditions: [terephthalic acid] (at t = -30 min) = 3 mM, [PFOA] (at t = -30 min) = 120 μM, same total surface area (1 m^2) of BN (1.25 g/L, S_{BET} = 40 m^2/g) or TiO_2 (0.5 g/L, S_{BET} = 100 m^2/g), ambient temperature, air headspace, initial pH 3.5, 254-nm light, photo flux = 6.5 × 10^{-6} Einstein·L^{-1}·s^{-1}.

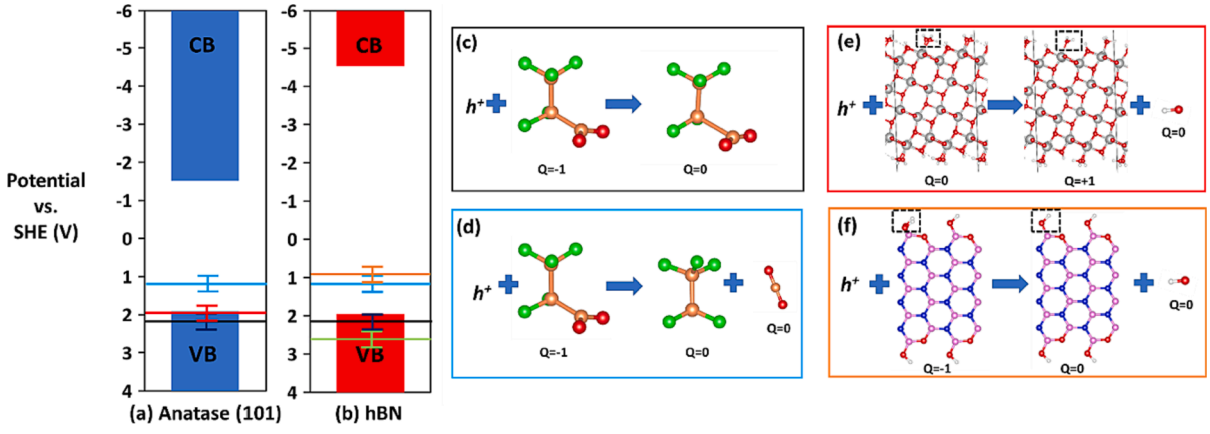

Fig. 5. (a) Calculated redox potentials of reactions over TiO_2: hole oxidation of surface hydroxyl (Eq. (4), red line), and of PFOA (Eq. (7), black line; and Eq. (8), blue line) and their positions relative to the band edge alignment of the anatase surface. (b) Calculated redox potentials of reactions in hBN system: hole oxidation of surface hydroxyl (Eq. (5), orange line) and of water (Eq. (6), green line), and of PFOA (Eq. (7), black line; and Eq. (8), blue line), and their positions relative to the band edge alignment of BN. An RMSE bar of 0.2 V is added, as benchmarked in our previous work.[24] Illustrations of (c) Eq. (7) reaction (black lines), (d) Eq. (8) reaction (blue lines), (e) Eq. (4) reaction (red line), and (f) Eq. (5) reaction (orange line). The black dotted boxes highlight the sites that change during the reactions. Atom colors: C (orange), F (green), O (red), H (white), Ti (grey), B (pink), and N (purple). (For interpretation of the references to colour in this figure legend, the reader is referred to the web version of this article.)

oxidize PFOA directly, [87,88] but can promote the degradation of PFCAs by reacting with perfluoroalkyl radicals (C_nF_{2n+1}•) [12,13]. We then estimated the generation of •OH radicals using the method described in Section 2.5, with an assumption of a 20 % trapping efficiency of TA [89,37]. As shown in Fig. 6, both materials generated •OH radicals during PFOA photocatalysis and more •OH radicals were accumulated over TiO_2. We calculated the hydroxyl radical formation rate with BN to be ~ 10 × lower than with TiO_2 (0.34 μM •OH/min *vs.* 3.5 μM •OH/min).

We can express the production rate of hydroxyl radical formation from hole consumption by surface hydroxyls as:

$$OH_{ad} + h^+ \overset{k_{\cdot OH}}{\rightarrow} \cdot OH \tag{19}$$

$$r_{\cdot OH} = k_{\cdot OH} \times C_{OH_{ad}} \times C_{holes} \tag{20}$$

The implication of this side reaction is that, in any system, surface hydroxyls will compete with PFOA for reaction with surface holes. The fact that the TiO_2 generates hydroxyl radicals 10 × faster than BN implies a much higher amount of surface hydroxyls on TiO_2 than on BN, which is expected given TiO_2's affinity for forming surface hydroxyls [81,83,84]. While these not only make TiO_2 more hydrophilic and less likely to adsorb PFOA, they also have the unintended negative consequence of consuming holes which could have reacted with PFOA molecules, compounding the inefficiency of the system. While we note hydroxyl radicals can be formed from hydrogen peroxide generated from the reaction of photogenerated superoxide radicals with a hole and a proton, [24,90] this is expected to be negligible as no intermediate hydrogen peroxide was detected using titanium(IV) oxysulfate reagent in this work.

4. Outlook

BN is a wide bandgap semiconductor that exhibits limitations in its ability to absorb light effectively. In our previous work, the combination of BN with wide bandgap TiO_2 facilitated the adsorption of UV-A light. Additionally, it resulted in the creation of a semiconductor heterojunction, facilitating the separation of electrons and holes. This property is particularly advantageous for the efficient degradation of PFOA, which occurred even under solar radiation.

This current work highlights a key limitation. TiO_2, which, being a hydrophilic material, exhibits a relatively slower rate of PFOA degradation due to poor PFOA adsorption and inefficient reactions of photogenerated holes with adsorbed hydroxyls. To further enhance BN photocatalyst performance for PFOA, future composites should incorporate hydrophobic wide bandgap semiconductor materials with complementary band structures.

5. Conclusion

Enhanced PFOA photodegradation performance of BN over TiO_2 was investigated in the present work, with a focus on the role of material hydrophobicity. BN was ~ 2.7 × faster at photocatalytically degrading PFOA than TiO_2 under 254-nm light illumination at near-neutral pH. Acidic pH accelerated PFOA (pre)adsorption and photodegradation for both materials due to improved electrostatic interactions between PFOA and the catalyst surfaces, and enhanced BN photocatalysis more (~3.5 × faster than TiO_2). PFOA sorption experiments showed hydrophobic BN had stronger PFOA adsorption affinity and ~ 2 × higher PFOA surface coverage for BN regardless of pH, affirming the positive benefit of surface hydrophobicity on catalysis. A Langmuir-Hinshelwood rate law comparison suggested hole surface concentrations were comparable, and DFT modeling indicated that holes on both photocatalysts were energetically capable of reacting with both surface hydroxyl groups and adsorbed PFOA. BN has less surface hydroxyls and more adsorbed PFOA than the presumably fully surface-hydroxylated TiO_2, such that BN surface hydrophobicity effectively directs the holes to react with physisorbed PFOA rather than with surface hydroxyls. In comparison, the holes of TiO_2 react more readily with surface hydroxyl groups than with PFOA, leading to the observed lower PFOA degradation rates and a higher OH formation rate. Thus, hydrophobicity of a photocatalyst surface contributes to higher degradation activity by increasing surface concentration of the target compound, and by diminishing the amount of surface hydroxyl groups which can react with the photogenerated holes.

CRediT authorship contribution statement

Bo Wang: Conceptualization, Investigation, Validation, Writing – original draft, Writing – review & editing. **Yu Chen:** Formal analysis, Investigation, Software, Writing – original draft. **Joshua Samba:** Investigation, Methodology, Validation. **Kimberly Heck:** Conceptualization, Supervision, Writing – original draft, Writing – review & editing. **Xiaochuan Huang:** Investigation, Validation. **Junseok Lee:** Investigation. **Jordin Metz:** Investigation. **Manav Bhati:** Investigation. **John Fortner:** Investigation. **Qilin Li:** Investigation. **Paul Westerhoff:** Investigation. **Pedro Alvarez:** Investigation. **Thomas P. Senftle:** Conceptualization, Funding acquisition, Writing – original draft, Supervision. **Michael S. Wong:** Conceptualization, Funding acquisition, Investigation, Supervision, Writing – original draft, Writing – review & editing.

Declaration of competing interest

The authors declare that they have no known competing financial interests or personal relationships that could have appeared to influence the work reported in this paper.

Data availability

Data will be made available on request.

Acknowledgments

This work was partially supported by the NSF Nanosystems Engineering Research Center for Nanotechnology-Enabled Water Treatment (EEC-1449500). M.S.W. acknowledges additional support from the Strategic Environmental Research and Development Program (SERDP) award ER 22-3258 and NSF (TI-2243301 and TI-2314154). T.P.S. acknowledges additional support from NSF (CHEM-2247729). We thank Prof. A. Martí for use of the DR-UV spectrometer. We thank Mr. H. Jacobs for DRIFTS data collection and analysis.

Appendix A. Supplementary data

Supplementary data to this article can be found online at https://doi.org/10.1016/j.cej.2024.149134.

References

[1] X. Liu, W. Wei, J. Xu, D. Wang, L. Song, B.-J. Ni, Photochemical decomposition of perfluorochemicals in contaminated water, *Water Res.*. Published Online (2020:) 116311.
[2] K. Prevedouros, I.T. Cousins, R.C. Buck, S.H. Korzeniowski, Sources, fate and transport of perfluorocarboxylates, Environ. Sci. Tech. 40 (1) (2006) 32–44.
[3] Y. Miao, X. Guo, D. Peng, T. Fan, C. Yang, Rates and equilibria of perfluorooctanoate (PFOA) sorption on soils from different regions of China, Ecotoxicol. Environ. Saf. 139 (2017) 102–108.
[4] S. Nakayama, K. Harada, K. Inoue, et al., Distributions of perfluorooctanoic acid (PFOA) and perfluorooctane sulfonate (PFOS) in Japan and their toxicities, Environ Sci an Int J Environ Physiol Toxicol. 12 (6) (2005) 293–313.
[5] J. Thompson, G. Eaglesham, J. Mueller, Concentrations of PFOS, PFOA and other perfluorinated alkyl acids in Australian drinking water, Chemosphere 83 (10) (2011) 1320–1325.

[6] K.A. Pike, P.L. Edmiston, J.J. Morrison, J.A. Faust, Correlation Analysis of Perfluoroalkyl Substances in Regional US Precipitation Events, Water Res. 190 (2021) 116685.
[7] N. Kudo, Y. Kawashima, Toxicity and toxicokinetics of perfluorooctanoic acid in humans and animals, J. Toxicol. Sci. 28 (2) (2003) 49–57.
[8] Y. Pan, Y. Zhu, T. Zheng, et al., Novel Chlorinated Polyfluorinated Ether Sulfonates and Legacy Per-/Polyfluoroalkyl Substances: Placental Transfer and Relationship with Serum Albumin and Glomerular Filtration Rate, Environ. Sci. Tech. 51 (1) (2017) 634–644.
[9] U.S.EPA. Drinking Water Health Advisories for PFAS Fact Sheet for Communities. Accessed June 23, 2022. https://www.epa.gov/system/files/documents/2022-06/drinking-water-ha-pfas-factsheet-communities.pdf.
[10] ATSDR (Agency for Toxic Substances and Disease Registry). Toxicological Profile for Perfluoroalkyls (Draft for Public Comment). Accessed November 2, 2018. https://www.atsdr.cdc.gov/toxprofiles/tp.asp?id=1117&tid=237.
[11] Published (2023).
[12] J. Wang, C. Cao, Y. Zhang, Y. Zhang, L. Zhu, Underneath mechanisms into the super effective degradation of PFOA by BiOF nanosheets with tunable oxygen vacancies on exposed (101) facets, Appl Catal B Environ. 286 (2021) 119911.
[13] J. Wang, C. Cao, Y. Wang, Y. Wang, B. Sun, L. Zhu, In situ preparation of pn BiOI@Bi5O7I heterojunction for enhanced PFOA photocatalytic degradation under simulated solar light irradiation, Chem. Eng. J. 391 (2020) 123530.
[14] Z. Li, P. Zhang, S. Tian, X. Li, In2O3 nanoporous nanosphere: A highly efficient photocatalyst for decomposition of perfluorooctanoic acid, Appl Catal B Environ. (2012) 125(none).
[15] B. Gomez-Ruiz, P. Ribao, N. Diban, M.J. Rivero, I. Ortiz, A. Urtiaga, Photocatalytic degradation and mineralization of perfluorooctanoic acid (PFOA) using a composite TiO2− rGO catalyst, J. Hazard. Mater. 344 (2018) 950–957.
[16] D. Huang, L. Yin, J. Niu, Photoinduced hydrodefluorination mechanisms of perfluorooctanoic acid by the SiC/Graphene catalyst, Environ. Sci. Tech. 50 (11) (2016) 5857–5863.
[17] B. Zhao, M. Lv, L. Zhou, Photocatalytic degradation of perfluorooctanoic acid with β-Ga2O3 in anoxic aqueous solution, J. Environ. Sci. 24 (4) (2012) 774–780, https://doi.org/10.1016/s1001-0742(11)60818-8.
[18] L. Duan, B. Wang, K. Heck, et al., Efficient photocatalytic PFOA degradation over boron nitride, Environ. Sci. Technol. Lett. 7 (8) (2020) 613–619.
[19] 3M™ Boron Nitride Cooling Fillers. https://www.3m.com/3M/en_US/design-and-specialty-materials-us/boron-nitride/.
[20] Saint-Gobain Boron Nitride Powder Solutions. https://www.bn.saint-gobain.com/products/powder-solutions.
[21] Momentive Softouch™ CC 6097 boron nitride. https://www.momentive.com/en-us/categories/emulsions/momentive-softouch-cc-6097.
[22] CeraGlide Boron Nitride Coatings. https://www.bn.saint-gobain.com/products/coatings.
[23] T. Salavati-Fard, B. Wang, Significant Role of Oxygen Dopants in Photocatalytic PFCA Degradation over h-BN, ACS Appl. Mater. Interfaces 13 (39) (2021) 46727–46737.
[24] Chen Y, Bhati M, Walls BW, Wang B, Wong MS, Senftle TP. Mechanistic Insight into the Photo-Oxidation of Perfluorocarboxylic Acid over Boron Nitride. *Env Sci Technol.* doi:10.1021/acs.est.2c01637.
[25] Z. Li, P. Zhang, T. Shao, J. Wang, L. Jin, X. Li, Different nanostructured In2O3 for photocatalytic decomposition of perfluorooctanoic acid (PFOA), J. Hazard. Mater. 260 (2013) 40–46.
[26] X. Li, P. Zhang, L. Jin, T. Shao, Z. Li, J. Cao, Efficient photocatalytic decomposition of perfluorooctanoic acid by indium oxide and its mechanism, Environ. Sci. Tech. 46 (10) (2012) 5528–5534.
[27] Z. Song, X. Dong, N. Wang, et al., Efficient photocatalytic defluorination of perfluorooctanoic acid over BiOCl nanosheets via a hole direct oxidation mechanism, Chem. Eng. J. 317 (2017) 925–934.
[28] M. Qanbarzadeh, D. Wang, M. Ateia, S.P. Sahu, E.L. Cates, Impacts of Reactor Configuration, Degradation Mechanisms, and Water Matrices on Perfluorocarboxylic Acid Treatment Efficiency by the UV/Bi3O(OH)(PO4)2 Photocatalytic Process, ACS ES&T Eng. 1 (2) (2020) 239–248, https://doi.org/10.1021/acsestengg.0c00086.
[29] S. Barisci, R. Suri, Electrooxidation of short-and long-chain perfluoroalkyl substances (PFASs) under different process conditions, J. Environ. Chem. Eng. 9 (4) (2021) 105323.
[30] M. Sörengård, E. Östblom, S. Köhler, L. Ahrens, Adsorption behavior of per-and polyfluoralkyl substances (PFASs) to 44 inorganic and organic sorbents and use of dyes as proxies for PFAS sorption, J. Environ. Chem. Eng. 8 (3) (2020) 103744.
[31] M. Park, S. Wu, I.J. Lopez, J.Y. Chang, T. Karanfil, S.A. Snyder, Adsorption of perfluoroalkyl substances (PFAS) in groundwater by granular activated carbons: Roles of hydrophobicity of PFAS and carbon characteristics, Water Res. 170 (2020) 115364.
[32] Duan L, Wang B, Heck KN, et al. Titanium oxide improves boron nitride photocatalytic degradation of perfluorooctanoic acid. *Chem Eng J*. Published online 2022:137735.
[33] D. Liu, Z. Xiu, F. Liu, et al., Perfluorooctanoic acid degradation in the presence of Fe (III) under natural sunlight, J. Hazard. Mater. 262 (2013) 456–463.
[34] M. Sörengård, V. Franke, R. Tröger, L. Ahrens, Losses of poly-and perfluoroalkyl substances to syringe filter materials, J. Chromatogr. A 1609 (2020) 460430.
[35] B. Nowack, F.G. Kari, S.U. Hilger, L. Sigg, Determination of dissolved and adsorbed EDTA species in water and sediments by HPLC, Anal. Chem. 68 (3) (1996) 561–566.
[36] H. Seshadri, S. Chitra, K. Paramasivan, P.K. Sinha, Photocatalytic degradation of liquid waste containing EDTA, Desalination 232 (1–3) (2008) 139–144.
[37] Y.B. Yin, K.N. Heck, C.L. Coonrod, et al., PdAu-catalyzed oxidation through in situ generated H2O2 in simulated produced water, Catal. Today 339 (2020) 362–370.
[38] G. Kresse, J. Furthmüller, Efficient iterative schemes for ab initio total-energy calculations using a plane-wave basis set, Phys. Rev. B 54 (16) (1996) 11169.
[39] G. Kresse, J. Furthmüller, Efficiency of ab-initio total energy calculations for metals and semiconductors using a plane-wave basis set, Comput. Mater. Sci 6 (1) (1996) 15–50.
[40] K. Mathew, V.S.C. Kolluru, S. Mula, S.N. Steinmann, R.G. Hennig, Implicit self-consistent electrolyte model in plane-wave density-functional theory, J. Chem. Phys. 151 (23) (2019) 234101.
[41] K. Mathew, R. Sundararaman, K. Letchworth-Weaver, T.A. Arias, R.G. Hennig, Implicit solvation model for density-functional study of nanocrystal surfaces and reaction pathways, J. Chem. Phys. 140 (8) (2014) 84106.
[42] M.C. Toroker, D.K. Kanan, N. Alidoust, L.Y. Isseroff, P. Liao, E.A. Carter, First principles scheme to evaluate band edge positions in potential transition metal oxide photocatalysts and photoelectrodes, PCCP 13 (37) (2011) 16644–16654.
[43] I.M. Nadeem, J.P.W. Treacy, S. Selcuk, et al., Water dissociates at the aqueous interface with reduced anatase TiO2 (101), J. Phys. Chem. Lett. 9 (11) (2018) 3131–3136.
[44] R. Martinez-Casado, G. Mallia, N.M. Harrison, R. Pérez, First-principles study of the water adsorption on anatase (101) as a function of the coverage, J. Phys. Chem. C 122 (36) (2018) 20736–20744.
[45] L.E. Walle, A. Borg, E.M.J. Johansson, et al., Mixed dissociative and molecular water adsorption on anatase TiO2 (101), J. Phys. Chem. C 115 (19) (2011) 9545–9550.
[46] R.W. Dorn, M.J. Ryan, T.-H. Kim, et al., Identifying the molecular edge termination of exfoliated hexagonal boron nitride nanosheets with solid-state NMR spectroscopy and plane-wave DFT calculations, Chem. Mater. 32 (7) (2020) 3109–3121.
[47] D.A. Armstrong, R.E. Huie, W.H. Koppenol, et al., Standard electrode potentials involving radicals in aqueous solution: inorganic radicals (IUPAC Technical Report), Pure Appl. Chem. 87 (11–12) (2015) 1139–1150.
[48] K.-U. Goss, The p K a values of PFOA and other highly fluorinated carboxylic acids, Environ. Sci. Tech. 42 (2) (2008) 456–458.
[49] L. Duan, B. Wang, K.N. Heck, et al., Titanium oxide improves boron nitride photocatalytic degradation of perfluorooctanoic acid, Chem. Eng. J. 448 (June) (2022) 137735, https://doi.org/10.1016/j.cej.2022.137735.
[50] C.A. Clark, K.N. Heck, C.D. Powell, M.S. Wong, Highly defective UiO-66 materials for the adsorptive removal of perfluorooctanesulfonate, ACS Sustain. Chem. Eng. 7 (7) (2019) 6619–6628.
[51] F. Chen, A. He, Y. Wang, et al., Efficient photodegradation of PFOA using spherical BiOBr modified TiO2 via hole-remained oxidation mechanism, Chemosphere 298 (2022) 134176.
[52] C. Xiong, W. Tu, Synthesis of water-dispersible boron nitride nanoparticles, Eur. J. Inorg. Chem. 2014 (19) (2014) 3010–3015.
[53] J. Qu, Q. Li, C. Luo, J. Cheng, X. Hou, Characterization of flake boron nitride prepared from the low temperature combustion synthesized precursor and its application for dye adsorption, Coatings 8 (6) (2018) 214.
[54] M. Kosmulski, E. Matijević, Zeta potential of anatase (TiO2) in mixed solvents, Colloids Surf. 64 (1) (1992) 57–65.
[55] D. Verhovšek, N. Veronovski, U. Lavrenčič Štangar, M. Kete, K. Žagar, M. Čeh, The synthesis of anatase nanoparticles and the preparation of photocatalytically active coatings based on wet chemical methods for self-cleaning applications, Int. J. Photoenergy 2012 (2012).
[56] Q. Xiang, G. Shan, W. Wu, H. Jin, L. Zhu, Measuring log Kow coefficients of neutral species of perfluoroalkyl carboxylic acids using reversed-phase high-performance liquid chromatography, Environ. Pollut. 242 (2018) 1283–1290.
[57] J. Xu, Z. Liu, D. Zhao, N. Gao, X. Fu, Enhanced adsorption of perfluorooctanoic acid (PFOA) from water by granular activated carbon supported magnetite nanoparticles, Sci. Total Environ. 723 (2020) 137757.
[58] W. Wang, A. Maimaiti, H. Shi, et al., Adsorption behavior and mechanism of emerging perfluoro-2-propoxypropanoic acid (GenX) on activated carbons and resins, Chem. Eng. J. 364 (2019) 132–138.
[59] F. Li, Z. Wei, K. He, et al., A concentrate-and-destroy technique for degradation of perfluorooctanoic acid in water using a new adsorptive photocatalyst, Water Res. 185 (2020) 116219.
[60] M.J. Klemes, Y. Ling, C. Ching, et al., Reduction of a tetrafluoroterephthalonitrile-β-cyclodextrin polymer to remove anionic micropollutants and perfluorinated alkyl substances from water, Angew Chemie. 131 (35) (2019) 12177–12181.
[61] A. Yang, C. Ching, M. Easler, D.E. Helbling, W.R. Dichtel, Cyclodextrin Polymers with Nitrogen-Containing Tripodal Crosslinkers for Efficient PFAS Adsorption, ACS Mater Lett. 2 (9) (2020) 1240–1245.
[62] R. Wang, C. Ching, W.R. Dichtel, D.E. Helbling, Evaluating the Removal of Per-and Polyfluoroalkyl Substances from Contaminated Groundwater with Different Adsorbents Using a Suspect Screening Approach, Published online, Environ Sci Technol Lett, 2020.
[63] W. Wang, Z. Zhou, H. Shao, S. Zhou, G. Yu, S. Deng, Cationic covalent organic framework for efficient removal of PFOA substitutes from aqueous solution, *Chem. Eng. J.*. Published Online (2020) 127509.
[64] Y. Yang, Z. Zheng, W. Ji, J. Xu, X. Zhang, Insights to perfluorooctanoic acid adsorption micro-mechanism over Fe-based metal organic frameworks: Combining computational calculation with response surface methodology, J. Hazard. Mater. 395 (2020) 122686.
[65] M.S. Hellsing, S. Josefsson, A.V. Hughes, L. Ahrens, Sorption of perfluoroalkyl substances to two types of minerals, Chemosphere 159 (2016) 385–391.

[66] Y. Feng, Y. Zhou, P.-H. Lee, K. Shih, Mineralization of perfluorooctanesulfonate (PFOS) and perfluorodecanoate (PFDA) from aqueous solution by porous hexagonal boron nitride: adsorption followed by simultaneous thermal decomposition and regeneration, RSC Adv. 6 (114) (2016) 113773–113780.
[67] W. Lei, D. Portehault, D. Liu, S. Qin, Y. Chen, Porous boron nitride nanosheets for effective water cleaning, Nat. Commun. 4 (1) (2013) 1–7.
[68] G. Lian, X. Zhang, H. Si, J. Wang, D. Cui, Q. Wang, Boron nitride ultrathin fibrous nanonets: one-step synthesis and applications for ultrafast adsorption for water treatment and selective filtration of nanoparticles, ACS Appl. Mater. Interfaces 5 (24) (2013) 12773–12778.
[69] D. Liu, W. Lei, S. Qin, K.D. Klika, Y. Chen, Superior adsorption of pharmaceutical molecules by highly porous BN nanosheets, PCCP 18 (1) (2016) 84–88.
[70] L.Y. Antipina, K.Y. Kotyakova, M.V. Tregubenko, D.V. Shtansky, Experimental and Theoretical Study of Sorption Capacity of Hexagonal Boron Nitride Nanoparticles: Implication for Wastewater Purification from Antibiotics, Nanomaterials 12 (18) (2022) 3157.
[71] A. Pakdel, C. Zhi, Y. Bando, T. Nakayama, D. Golberg, Boron nitride nanosheet coatings with controllable water repellency, ACS Nano 5 (8) (2011) 6507–6515.
[72] A. Pakdel, X. Wang, Y. Bando, D. Golberg, Nonwetting, “white graphene” films, Acta Mater. 61 (4) (2013) 1266–1273.
[73] H. Li, X.C. Zeng, Wetting and interfacial properties of water nanodroplets in contact with graphene and monolayer boron–nitride sheets, ACS Nano 6 (3) (2012) 2401–2409.
[74] G.-X. Li, Y. Liu, B. Wang, X.-M. Song, E. Li, H. Yan, Preparation of transparent BN films with superhydrophobic surface, Appl. Surf. Sci. 254 (17) (2008) 5299–5303.
[75] Q. Ye, P.Y. Liu, Z.F. Tang, L. Zhai, Hydrophilic properties of nano-TiO2 thin films deposited by RF magnetron sputtering, Vacuum 81 (5) (2007) 627–631.
[76] M. Takeuchi, G. Martra, S. Coluccia, M. Anpo, Verification of the photoadsorption of H2O molecules on TiO2 semiconductor surfaces by vibrational absorption spectroscopy, J. Phys. Chem. C 111 (27) (2007) 9811–9817.
[77] A. Pakdel, Y. Bando, D. Golberg, Plasma-assisted interface engineering of boron nitride nanostructure films, ACS Nano 8 (10) (2014) 10631–10639.
[78] X. Li, H. Qiu, X. Liu, J. Yin, W. Guo, Wettability of supported monolayer hexagonal boron nitride in air, Adv. Funct. Mater. 27 (19) (2017) 1603181.
[79] Smith McWilliams AD, Martínez-Jiménez C, Matatyaho Ya'akobi A, et al. Understanding the Exfoliation and Dispersion of Hexagonal Boron Nitride Nanosheets by Surfactants: Implications for Antibacterial and Thermally Resistant Coatings. *ACS Appl Nano Mater*. 2021;4(1):142-151.
[80] B.R. Shah, U.D. Patel, Mechanistic aspects of photocatalytic degradation of Lindane by TiO2 in the presence of Oxalic acid and EDTA as hole-scavengers, J. Environ. Chem. Eng. 9 (4) (2021) 105458.
[81] H. Shibata, Y. Ogura, Y. Sawa, Y. KoNo, Hydroxyl radical generation depending on O2 or H2O by a photocatalyzed reaction in an aqueous suspension of titanium dioxide, Biosci. Biotech. Bioch. 62 (12) (1998) 2306–2311.
[82] T. Hirakawa, K. Yawata, Y. Nosaka, Photocatalytic reactivity for O2− and OH radical formation in anatase and rutile TiO2 suspension as the effect of H2O2 addition, Appl. Catal. A 325 (1) (2007) 105–111.
[83] Y. Nosaka, A. Nosaka, Understanding hydroxyl radical (• OH) generation processes in photocatalysis, ACS Energy Lett. 1 (2) (2016) 356–359.
[84] J. Zhang, Y. Nosaka, Photocatalytic oxidation mechanism of methanol and the other reactants in irradiated TiO2 aqueous suspension investigated by OH radical detection, Appl Catal B Environ. 166 (2015) 32–36.
[85] R. Omidirad, K. Azizi, DFT study of charge-controlled mechanism of water molecule dissociation on vacancy defected boron nitride nanosheets, J. Mol. Graph. Model. 93 (2019) 107448.
[86] C.E. Patrick, F. Giustino, Structure of a water monolayer on the anatase TiO 2 (101) surface, Phys. Rev. Appl 2 (1) (2014) 14001.
[87] H. Javed, C. Lyu, R. Sun, D. Zhang, P.J.J. Alvarez, Discerning the inefficacy of hydroxyl radicals during perfluorooctanoic acid degradation, Chemosphere 247 (2020) 125883.
[88] S.M. Mitchell, M. Ahmad, A.L. Teel, R.J. Watts, Degradation of perfluorooctanoic acid by reactive species generated through catalyzed H2O2 propagation reactions, Environ. Sci. Technol. Lett. 1 (1) (2014) 117–121.
[89] N. Milan-Segovia, Y. Wang, F.S. Cannon, R.C. Voigt, J.C. Furness, Comparison of hydroxyl radical generation for various advanced oxidation combinations as applied to foundries, Ozone Sci. Eng. 29 (6) (2007) 461–471.
[90] Y. Nosaka, A.Y. Nosaka, Generation and detection of reactive oxygen species in photocatalysis, Chem. Rev. 117 (17) (2017) 11302–11336.